GEOPHYSICS, VOL. 77, NO. 3 (MAY-JUNE 2012); P. E227–E237, 15 FIGS.
10.1190/GEO2010-0194.1

Data error quantification in spectral induced polarization imaging

Adrián Flores Orozco[1], Andreas Kemna[2], and Egon Zimmermann[3]

ABSTRACT

Induced polarization (IP) imaging is being increasingly used in near-surface geophysical studies, particularly for hydrogeologic and environmental applications. However, the analysis of IP data error has received little attention, even though the importance of an adequate error parameterization has been demonstrated for electrical resistivity imaging. Based on the analysis of data sets measured in the frequency range from 1 Hz to 1 kHz, we proposed a model for the quantification of phase data errors in IP measurements. The analyzed data sets were collected on an experimental tank containing targets of different polarizability. Our study is based on the common practice that the discrepancy of measurements taken in normal and reciprocal configuration can be considered as a measure of data error. Statistical analysis of the discrepancies between normal and reciprocal measurements revealed that the phase error decreases with increasing resistance (i.e., signal strength). We proposed an inverse power-law model to quantify the phase error as a function of the measured resistances. We found that the adequate implementation of the proposed error model in an inversion scheme leads to improved IP imaging results in laboratory experiments. Application to a data set collected at the field-scale also demonstrated the superiority of the new model over previous assumptions.

INTRODUCTION

Induced polarization (IP) imaging has emerged as a promising method for hydrogeologic and environmental studies. In recent years, several laboratory studies have demonstrated the capability of the IP method to gain valuable information about textural and hydraulic properties of the subsurface (e.g., Binley et al., 2005; Zisser et al., 2010). At the field-scale, it has been demonstrated that IP imaging can lead to improved lithological characterization (e.g., Kemna et al., 2004; Hördt et al., 2009; Slater et al., 2010) and detection of contaminants (e.g., Kemna et al., 2004). It also has been used for the monitoring of geochemical and biogeochemical processes (e.g., Slater and Binley, 2006; Williams et al., 2009). This is due to the fact that IP measurements provide information not only about conduction (resistivity method), but also about the capacitive properties of the subsurface. Moreover, measurements collected at different frequencies (referred to as spectral induced polarization [SIP]) might also provide information about geometrical properties of the pore space (e.g., Pelton et al., 1978; Wong, 1979; Binley et al., 2010; Revil and Florsch, 2010). However, applications of SIP imaging at the field-scale are still rare because of the limitations and difficulties associated with data acquisition, and the lack of studies regarding the parameterization of data error in inversion schemes.

Every measurement is subject to systematic and random errors. In the case of electrical methods, the former are commonly associated with problems during data acquisition such as poor galvanic contact, malfunction of the measuring device, and some sources of anthropogenic noise. There are particular effects that need to be considered as sources of systematic errors for SIP measurements. These include polarization of the electrodes used for current injection (Dahlin et al., 2002; LaBrecque and Daily, 2008), primarily for measurements at lower frequencies (<10 Hz), and electromagnetic coupling (capacitive and inductive effects), which is more significant for measurements at higher frequencies (>10 Hz), associated with the wires connecting the electrodes and the measuring device (e.g., Pelton et al., 1978). However, this study does not address systematic errors, because it is assumed that they need to be avoided or corrected before the inversion.

Random errors cannot be predicted as they arise primarily from fluctuations in the contact between the electrodes with the ground/air, and in the injected current and its pathways (e.g., Binley et al., 1995; LaBrecque et al., 1996; Slater et al., 2000). Previous studies

Manuscript received by the Editor 25 June 2010; revised manuscript received 13 December 2011; published online 27 April 2012.
[1] Formerly Agrosphere (IBG 3), Forschungszentrum Jülich GmbH, Jülich, Germany; presently University of Bonn, Department of Geodynamics and Geophysics, Bonn, Germany. E-mail: flores@geo.uni-bonn.de.
[2] University of Bonn, Department of Geodynamics and Geophysics, Germany. E-mail: kemna@geo.uni-bonn.de.
[3] Central Institute for Electronics (ZEL), Jülich, Germany. E-mail: E.Zimmermann@FZ-Juelich.de.

have demonstrated that adequate estimation of random errors in tomographic data sets plays an important role regarding the quality of the resultant electrical images (e.g., Binley et al., 1995; LaBrecque et al., 1996). Even though the advantage of a proper error description in the inversion has been demonstrated for resistance data sets (e.g., Binley et al., 1995; LaBrecque et al., 1996), there have not yet been any studies investigating this issue for IP or SIP. So far, a constant error of the phase of the measured impedance has been assumed (Kemna, 2000), ignoring a possible dependence of the phase error on resistance (reflecting voltage signal strength for constant current) or the phase value itself.

The objective of this study is to improve SIP imaging by establishing an appropriate error model for the inversion of phase data based on a thorough analysis of tomographic impedance data sets measured in the laboratory under controlled conditions. Taking into account the fact that the numerical modeling of typical noise characteristics is practically impossible due to its complexity and the various possible sources, our analysis is based on performed (real) measurements and not on synthetic data.

The first section of the study addresses how data error is incorporated in the complex resistivity inversion scheme and which error models have been used so far for the description of resistance and phase errors. The second section presents the experimental setup and measurement scheme, a thorough analysis of the (spectral) raw data, a new phase error model, and the imaging results obtained. The third section shows the application of the proposed phase error model to single-frequency field data, followed by discussion and conclusions.

DATA ERROR TREATMENT IN COMPLEX RESISTIVITY IMAGING

Complex resistivity inversion scheme

The complex resistivity images presented in this work were computed using the smoothness-constraint inversion code by Kemna (2000). Based on a finite-element discretization, the code calculates the distribution of complex resistivity, $\rho = |\rho|e^{i\phi}$ (with magnitude ($|\rho|$) and phase (ϕ), and $i = \sqrt{-1}$), in a 2D image plane from a given data set of transfer impedances Z_j ($j = 1, \ldots, n$; with n being the number of measurements) measured at some frequency f. The underlying forward model solves either the Helmholtz equation in the wavenumber domain for a 2.5D modeling problem, or the Poisson equation in real space for a purely 2D modeling problem.

The inversion algorithm iteratively minimizes an objective function composed of the measures of data-misfit and first-order model roughness, with both terms being balanced by a regularization parameter. The iteration process is stopped when the rms data-misfit value,

$$\mathrm{rms} = \sqrt{\frac{1}{n}\sum_{j=1}^{n}\frac{|d_j - f_j(\mathbf{m})|^2}{|\varepsilon_j|^2}} \qquad (1)$$

reaches the value of one for the smoothest possible model. In equation 1, $\mathbf{m}$ represents the model vector (here log-transformed complex resistivity), $f_j(\mathbf{m})$ the operator of the forward model, d_j the jth datum (here log-transformed complex impedance) with error ε_j. In the inversion algorithm, it is assumed that the data errors are uncorrelated and normally distributed. The complex data error ε_j can be considered as a confidence region ellipse in the complex plane around the data point d_j, expressed as

$$\varepsilon_j = s(\ln|Z_j|) + is(\phi_j), \qquad (2)$$

where $s(\ln|Z_j|)$ and $s(\phi_j)$ represent the standard deviations of the log magnitude $\ln|Z_j|$ and phase ϕ_j, respectively, of the impedance Z_j (note that $d_j = \ln Z_j = \ln|Z_j| + i\phi_j$). In the complex error, $s(\ln|Z_j|)$ typically dominates $s(\phi_j)$ and thus controls the inversion behavior (and stopping criterion) of the complex-valued inversion scheme. To take the phase error into account quantitatively, additional, real-valued inversion iterations are run only for the phase data, once the complex inversion has reached an rms of one. The iterative inversion process for the phase is stopped when the corresponding rms (for the phase inversions) value,

$$\mathrm{rms}_{\mathrm{phase}} = \sqrt{\frac{1}{n}\sum_{j=1}^{n}\left(\frac{\mathrm{Im}(d_j) - \mathrm{Im}(f_j(\mathbf{m}))}{s(\phi_j)}\right)^2}, \qquad (3)$$

reaches the value of one for the smoothest possible model. For further details on the inversion algorithm, as well as the underlying finite-element forward modeling, we refer to Kemna (2000).

Parameterization of resistance error

The final result of the inversion strongly depends on the data error and its parameterization. However, it is practically impossible to know the exact variance and distribution of the random errors in the data. It is, therefore, necessary to make use of approximations to characterize the data error for the inversion (LaBrecque et al., 1996).

LaBrecque et al. (1996) proposed a linear relationship between the measured resistances (denoted as $R = |Z|$ in the following) and their associated error, $s(R)$). This model can be written (e.g., Slater et al., 2000) as

$$s(R) = a + bR, \qquad (4)$$

where a is the absolute resistance error at small resistance values ($R \to 0 : s(R) = a$), and b defines the relative (percentage) resistance error for larger resistance values ($R \to \infty : s(R) = bR$). The parameters a and b can be estimated from the standard deviation of the difference (ΔR) between normal (R_n) and reciprocal (R_r) measurements in the data set (LaBrecque et al., 1996). Reciprocal measurements are those collected when current and potential dipoles are interchanged from the "normal" configuration.

Parameterization of phase error

In contrast to resistivity imaging, only a few studies have dealt with the analysis of the error present in impedance phase measurements. In the first reported work (Ramirez et al., 1999), the authors based their study on the analysis of reciprocal measurements, analogous to LaBrecque et al. (1996). They performed measurements in a tank with different targets and presented plots of the calculated absolute value of the discrepancy in the phase ($|\Delta\phi|$), given by the difference between normal (ϕ_n) and reciprocal (ϕ_r) phase measurements, against the corresponding average value. Based on the observed distribution of the phase discrepancy, they defined

a constant value to describe the error in the phase data, which encompasses most of the measurements. In their study, the authors also reported a noticeable increase in the phase discrepancy for data collected at high frequencies, indicating a frequency dependence of the phase error.

The second approach, by Slater and Binley (2006), is based on a statistical analysis of the difference between normal and reciprocal measurements ($\Delta\phi$, not $|\Delta\phi|$). Slater and Binley (2006) calculated the standard deviation of the entire data set and used this value to define a constant-phase error ($s(\phi)$) in the inversion. The images presented show negligible artifacts and a good correlation with the expected models. However, the data in their study were originally collected in the time domain and the measured chargeabilities were, as a first approximation, linearly converted to phase values for the inversion in the frequency domain. Therefore, the presented plots of normal-reciprocal discrepancies in the IP data may only provide limited insight into the error characteristics of true phase measurements.

ANALYSIS OF SPECTRAL DATA FROM A LABORATORY EXPERIMENT

Experimental setup and measurement scheme

To study the characteristics of random error in SIP phase measurements, we collected several tomographic data sets on a physical tank model. The Plexiglas tank has a length of 1 m, a width of 0.5 m, and a height of 0.02 m, and was uniformly filled with well-characterized quartz sand and tap water (as saturating electrolyte). Two filters made of porous polyethylene (with a pore diameter of approximately 200 μm) were installed (0.1 m away from the edges, as depicted in Figure 1) to allow dynamic flow experiments in the tank with a homogeneous flow field. However, the measurements presented here were collected under static (no-flow) conditions.

Altogether, 80 pin electrodes, made of copper with a diameter of 4 mm, were installed along the long walls of the tank (40 on each side) at a constant spacing of 2.5 cm (Figure 1). The electrodes were mounted into the walls of the tank as depicted in Figure 1 to reduce the contact of the electrodes inside the tank and to fulfill the assumption of point electrodes as required in the inversion. Taking into account the geometry of our electrodes, we estimated an error below 5% for the "worst" case of injecting current at a single electrode and measuring the potential magnitude at an adjacent electrode (note that there is no such error for the phase of the potential), based on the analytical solution provided in Militzer and Weber (1985). This systematic error rapidly decreases for larger distances from the current electrode.

Three different targets were placed inside the saturated-sand background to build a model with some degree of complexity. Moreover, different materials were selected as targets to enhance different polarization mechanisms, i.e., massive copper associated with electrode polarization at the metal-electrolyte interface and pure clay associated with so-called membrane polarization at the clay mineral-electrolyte interface. Generally, electrode polarization has a larger magnitude than membrane polarization (e.g., Pelton et al., 1978; Slater et al., 2006). More explicitly, the targets were: (1) a 0.1 m diameter copper cylinder, (2) a 0.1 m diameter clay cylinder, and (3) a 0.075 m thick clay "layer."

Our laboratory study was designed as a 2D experiment to better evaluate the imaging result, to simplify the measuring protocols, and to reduce data acquisition times (critical for SIP measurements at low frequencies). However, the presented data analysis approach is analogously applicable to 3D data sets. To satisfy the assumption of a 2D case, we avoided changes in the third dimension (the height of the tank). It was achieved in the following way: (1) the tank contained targets, filters and filling materials that extended uniformly along the tank height; (2) current injection and measurements of electrical potential were performed on line electrodes extending along the entire height of the tank, afterward the collected resistance values of the electrical impedance were normalized by this height. From symmetry, the deployment of line electrodes results in electrical fields that vary only in two dimensions, and therefore can be modeled with our 2D inversion approach. To illustrate the accuracy of the 2D forward modeling underlying the inversion algorithm for the given measurement geometry, Figure 2 shows a comparison between the numerical and analytical solution for an exemplary injection dipole assuming a constant resistivity inside the tank. The potential distribution reflects the no-flow boundary conditions imposed everywhere on the tank boundary. In the analytical solution, the no-flow conditions at the four edges were accounted for by computing the superposed potential for 800 fictitious "mirror" sources (see, for example, Weidelt and Weller [1997] for the computation of the analytical solution for a point source on the boundary of a confined body).

An impedance spectrometer with high phase accuracy, described in detail in Zimmermann et al. (2008), was used to perform the

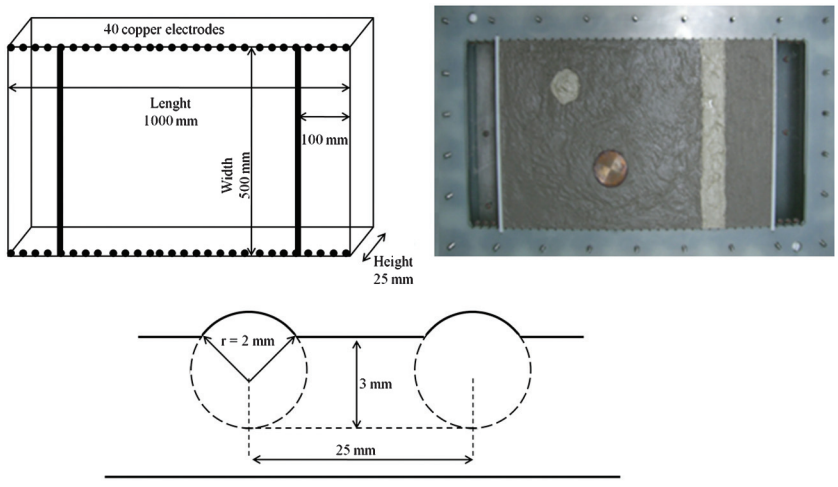

Figure 1. Top left: Schematic representation of the 2D tank with 80 electrodes. Top right: Photo of the tank with the targets (anomalies) inside: two cylindrical bodies (10 cm radius) made of clay and copper, and a 5 cm clay layer. Quartz sand was used to fill the rest of the tank between the filters, and tap water was used as electrolyte. Bottom: Schematic representation of the electrodes (dashed circles) and their emplacement in the insulating walls of the tank (represented by solid lines), to reduce the effective width of the electrodes (solid arcs). Less than one third of the total electrode area was used to perform measurements, validating the ideal-line-electrode assumption in the numerical modeling.

measurements. The equipment has 32 channels for current injection and 92 channels to collect electrical impedance data in the frequency domain. To avoid cross-talking between the cables and to reduce electromagnetic coupling, coaxial cables were used to connect the electrodes in the tank with the equipment. The electronic component (to inject the current or to perform potential measurements) was placed at the end of each cable, connected directly to the electrodes (1 cm distance between electrode and electronic component). The tank and the measuring equipment were separated from the other electrical devices to avoid electromagnetic contamination of the data.

The resolution of the imaging results depends on the measurement configuration. This issue has been addressed in numerous studies for synthetic and field data (e.g., Xu and Noel, 1993; Bing and Greenhalgh, 2000; Slater et al., 2000; Stummer et al., 2004). In the present study, two different measuring configurations were used. In the first configuration (hereafter referred to as cross dipoles), the current dipole was placed on one side of the tank and the voltage dipole on the other (as depicted in Figure 3). The measurements were performed using standard skip-1 ("1" denoting the number of electrodes that are "skipped" by each dipole) and skip-2 dipole-dipole schemes. This resulted in a total of 2600 measurements (1300 normal, 1300 reciprocal).

In the second configuration (hereafter referred to as opposite dipoles), the current and voltage dipoles were opposite each other in the tank, i.e., current source (C+) and positive potential (P+) were located on one side, and current sink (C−) and negative potential (P−) on the other, as depicted in Figure 3. The total number of measurements here was 950 (475 normal, 475 reciprocal).

The selected configurations minimized the risk of systematic errors due to polarization of the electrodes and provided a wide range in the measured resistance values, corresponding to a wide range in the signal-to-noise ratio (S/N), which allows the proper investigation of the relationship between phase error and resistance value.

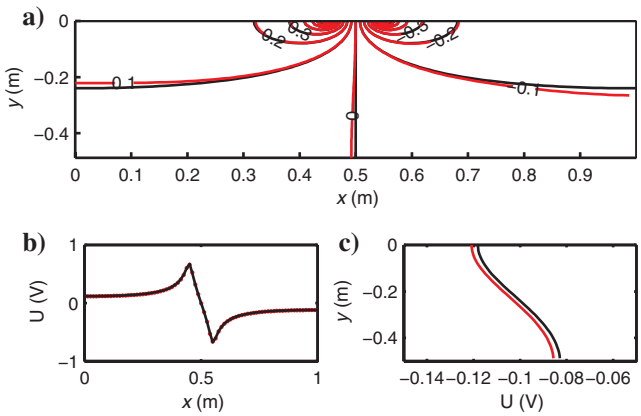

Figure 2. 2D modeled numerical (red lines) and analytical (black lines) distribution of the electrical potential inside the tank due to an electric current dipole (indicated by the solid circles). The potential (U) values of plotted equipotential lines are given in V, for a current of 1 A and a background resistivity of 1 Ωm (Figure 2a). The potential distributions along the right ($x = 1$ m) and close to the top ($y = -0.125$ m) boundaries are also presented (Figure 2b and 2c, respectively). The analytical solution was computed by superposition of the potential of 800 fictitious mirror sources to account for the no-flow boundary conditions along the four edges of the tank.

In addition to the collection of normal and reciprocal data, i.e., exchanging C+ with P+ and C− with P−, the measurement system used repeats each measurement with swapped current injection polarity, i.e., internally exchanges C+ with C−. Zimmermann et al. (2008) showed that averaging the corresponding measurements eliminates the negative effect of parasitic currents. Data were collected at frequencies between 1 Hz and 1 kHz. At lower frequencies, overall data acquisition time becomes relatively long, while at higher frequencies systematic errors due to electromagnetic coupling start to occur (Zimmermann et al., 2008).

Data analysis and new phase error model

As in previous studies (Binley et al., 1995; LaBrecque et al., 1996; Slater and Binley, 2006), we analyzed the discrepancy between normal and reciprocal measurements, assuming that this represents a practical measure of data error. The plots of the normal-reciprocal discrepancies in the resistance (ΔR) against the corresponding resistance value (R) (Figure 4, left column) behave as described by the model proposed by LaBrecque et al. (1996) (equation 4; note that in Figure 4, ΔR is plotted against log R to better resolve the distribution of data points). No significant change is observed in the resistance behavior for the different frequencies (Figure 4, left column). For the phase measurements, the data collected with the opposite dipoles configurations show a high S/N, characterized by a low value in the normal-reciprocal discrepancy of the phase. In contrast, the measurements performed with the cross dipoles configuration exhibit larger phase values and larger normal-reciprocal phase discrepancies (Figure 4, middle and right-hand columns).

Our first approach to describe the error in the phase measurements was based on a relationship between the normal-reciprocal phase discrepancy ($\Delta\phi$) and the absolute value of the phase ($|\phi|$), similar to the study of Ramirez et al. (1999). However, as shown in the middle column of Figure 4, the plots exhibit a scattered distribution. Therefore it does not seem appropriate to characterize the phase discrepancy as a function of the phase value. Also the absolute phase discrepancy ($|\Delta\phi|$) as a function of the absolute phase value was studied with no better results (plots not shown).

Given the expected correlation between resistance and signal strength, and signal strength and phase error, we then analyzed

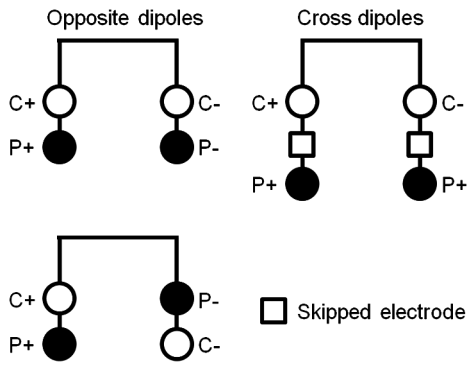

Figure 3. Measurement configurations used to collect data for the 2D tank experiment. Left: "Opposite dipoles" configuration. Right: "Cross dipoles" configuration. Current electrodes (C+, C−) are indicated by open circles and potential electrodes (P+, P−) by solid circles.

the distribution of the phase discrepancy against the corresponding resistance value. Here, a systematic trend is noticeable (Figure 4, right-hand column): higher phase discrepancies are associated with lower resistances and vice versa. If only the phase data recorded at high resistance values were considered, the error for the phase could be described fairly well by a constant value (Figure 4, right column), in accordance with previous approaches (Kemna, 2000; Slater and Binley, 2006). However, rejecting the data with low resistance values would reduce the data set by more than 65% leading to a loss of resolution of the inverted phase image. Therefore, and to account for the large dynamics in the resistance data, it is reasonable to consider the error in the phase measurements as a function of resistance.

For SIP measurements, it is essential to take into consideration the distribution of the phase discrepancies at different frequencies. Here, the plots of the phase discrepancy as a function of resistance display a consistent behavior for all frequencies, as shown in Figure 4. Based on the observed distribution of the phase discrepancies, we propose an inverse power-law relationship between the error in the phase ($s(\phi)$) and the corresponding resistance (R)

$$s(\phi) = aR^b, \tag{5}$$

with $b < 0$. For $b \to 0$, the proposed model reduces to the constant-phase error model used in previous studies (Kemna, 2000; Slater and Binley, 2006).

To calculate the a and b parameters of the phase error model in equation 5, as well as the a and b parameters of the resistance error model in equation 4, we performed a so-called bin analysis. This technique was used by Koestel et al. (2008) to describe the error in ERT data sets. The procedure is based on the partition of the data set into several bins with respect to the resistance value. Each bin contains the normal-reciprocal phase and resistance discrepancies, respectively, of those data whose resistances fall into the resistance range of the bin. Once the data are sorted in these bins, the standard deviation of the corresponding discrepancies is calculated. Finally, the assumed error model is fitted to the standard deviations of the different bins as a function of the corresponding mean resistance value. The obtained parameters a and b are then used to describe the phase and resistance errors, respectively, according to the assumed model, in the inversion. This procedure was applied here for each of the data sets collected at the different frequencies.

The bin analysis is based on the assumption that the discrepancy values contained in each bin obey a normal distribution, so that they can be described by its standard deviation. To prove whether this assumption is justified we plotted the histograms of the resistance and phase discrepancy values for selected bins, based on different total numbers of bins. Examples of histograms for a selected bin (in this case the fourth bin) for different numbers of bins are shown in Figure 5, for different measurement frequencies. It is obvious that the distribution of data points depends on the number of bins defined in the analysis. Sampling with a high number of bins (here 42) leads to gaps in the histograms, due to the relatively small number of data points in the individual bins or even empty bins, which no longer obey a normal distribution. Sampling with a low number of bins (here 8) no longer follows a Gaussian-like behavior and is also insufficient to capture the dynamics in the error.

Therefore, it is important to select an adequate number of bins for the given number of measurements and range of resistances. To illustrate this issue, we plotted the calculated phase error model (equation 5) for different numbers of bins (Figure 6). Here we see that at low frequencies, the deviations between the obtained curves are generally relatively small. Larger deviations occur for low resistances and higher frequencies, the latter reflecting the increase of the normal-reciprocal phase discrepancies with frequency (Figure 4). However, the error models for a moderate number of bins capture the mean behavior of the curves for all analyzed frequencies, demonstrating the robustness of the approach. Importantly, the phase error model differs significantly from the

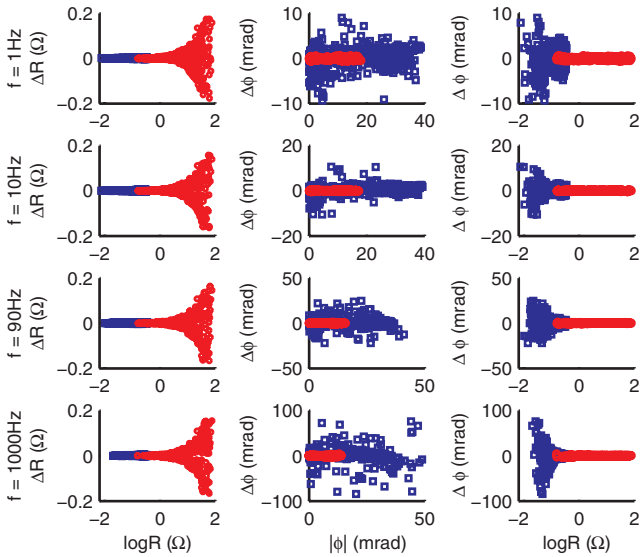

Figure 4. Raw tank data collected at different frequencies for both measurement schemes (blue squares: opposite dipoles; red circles: cross dipoles). Left column: Normal-reciprocal resistance discrepancy versus log resistance. Middle column: Normal-reciprocal phase discrepancy versus absolute phase. Right column: Normal-reciprocal phase discrepancy versus log resistance.

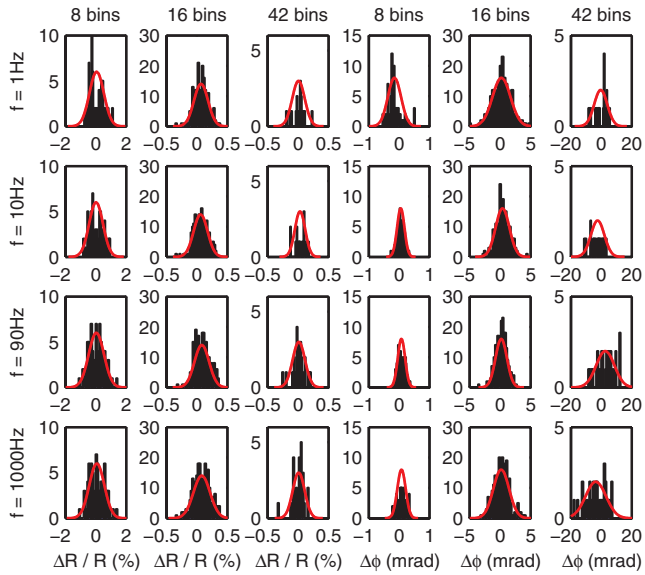

Figure 5. Histograms of the normal-reciprocal discrepancies of the resistance and phase tank data in the fourth bin based on different numbers of bins used in the analysis (eight, 16, and 42 bins).

constant-phase error model ("single-bin" approach) according to Slater and Binley (2006).

For the results presented here, the bin analysis was performed using equally sized bins based on a logarithmic resistance scale. This sampling provided a fairly even distribution of data points over the bins. In the following, 16 bins were used for the analysis. This is the maximum number of bins for which each bin still contains at least 2% of the total number of measurements.

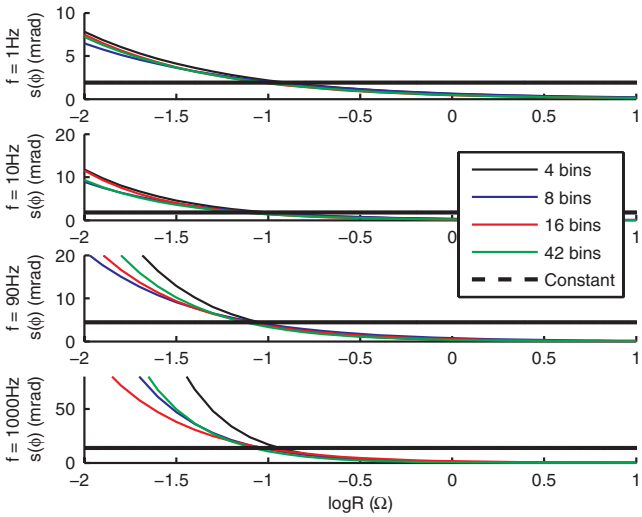

Figure 6. Calculated phase error models according to equation 5 for the tank data using different numbers of bins in the underlying analysis. For comparison, the constant-phase error model based on a single-bin analysis according to Slater and Binley (2006) is shown.

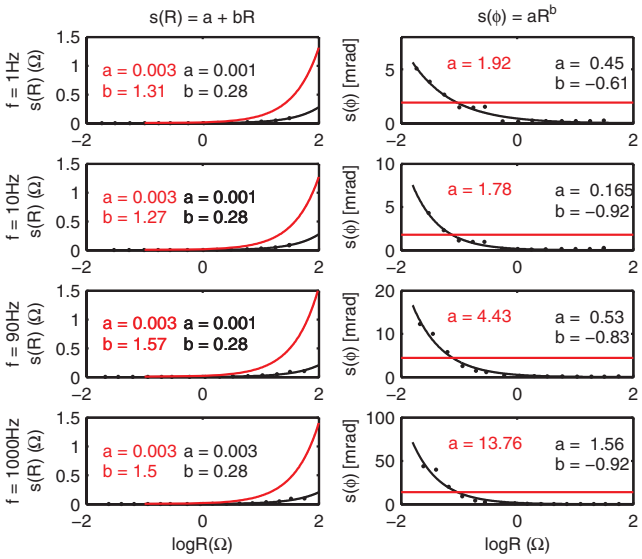

Figure 7. Resistance (left) and phase (right) error models for the tank data at different measurement frequencies based on a multibin analysis (black curves) and the single-bin approach by Slater and Binley (2006) (red curves). The black dots indicate the obtained standard deviations of the normal-reciprocal data discrepancies in the individual bins. Also shown are the corresponding values of the error model parameters a and b (for resistance, a in Ω and b in %; for phase, a in mrad and b value for R in Ω).

Imaging results

In this section, we present the imaging results obtained with the error models in equations 4 and 5 for the measurements collected in the tank. Figure 7 shows the corresponding resistance and phase error models computed for the data sets at different frequencies, in comparison with the models obtained from the single-bin approach by Slater and Binley (2006).

For the inversion, we used a regular grid of square elements. The size of the elements was given by half of the distance between adjacent electrodes (1.25 cm). Images also were calculated with error parameters determined according to the approach of Slater and Binley (2006) and are shown for comparison. The resistivity magnitude image obtained after the inversion of the 1 Hz tank data is shown in Figure 8. It does not make any noticeable difference whether the error parameters are defined based on a single- or a multibin analysis, although the parameter values are different (see Figure 7). In the image, the lowest resistivity values occur in the areas beyond the filters in the tank, where only tap water is present (resistivity below 15 Ωm), whereas the highest resistivity values are found in the area between the filters, where the quartz sand is located (resistivity above 30 Ωm). The three targets as well as the filters are reasonably recovered in position and extension (cf. Figure 1). Minor artifacts can be identified in the area close to the filter on the left, but these are probably due to air bubbles present during data acquisition. We note that the resistivity images obtained for other measurement frequencies are effectively the same and are thus not shown.

Figure 9 shows the images obtained from the inversion of the phase data at different frequencies. With both error approaches, the copper target is reasonably well recovered (except for the highest frequency) as a high-polarizable anomaly (up to 100 mrad) at the correct location. Below 1 kHz, the phase images calculated with the proposed phase error model clearly show fewer artifacts than those obtained with the constant-phase error model (suggesting an overfitting of the data for the latter). At 1 kHz, the constant-phase error

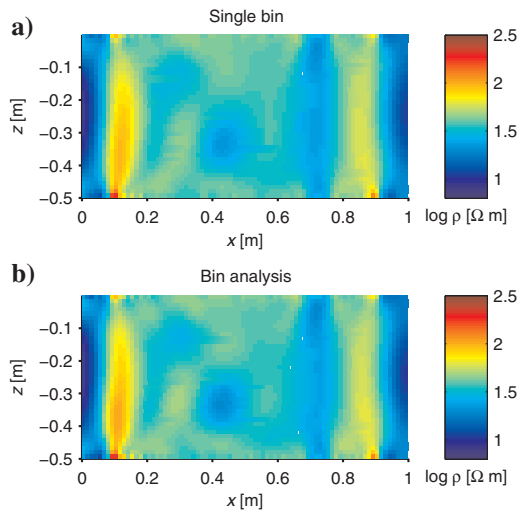

Figure 8. Resistivity magnitude image inverted from the 1 Hz tank data using the error model in equation 4 with parameters based on the Slater and Binley (2006) approach (a) and a multibin analysis according to Koestel et al. (2008) (b).

model yields a very smooth image in which no anomalies are visible at all (suggesting an underfitting of the data), while the new error model produces an image in which the target still can be located. The clay targets, on the other hand, are not visible at all in the images based on the constant-phase error description, while at least the "clay layer" target is indicated for the higher frequencies toward the boundaries of the images obtained with the proposed phase error model. However, the clay targets obviously are difficult to detect because their response is much weaker than that of the copper target and they are hence masked in the imaging. The background material in the tank (sand saturated with tap water) exhibits low polarizability (few milliradians), as expected.

To better examine the imaging results in terms of the recovered frequency dependence, pixel values were picked from the phase images at the different frequencies at the locations of the polarizable copper target and the clay layer target (Figure 10). For both pixels (targets), a systematic spectral behavior is observed, in particular for the spectra based on the proposed phase error model. In the frequency range considered, the reconstructed phase values for the copper target decrease continuously with increasing measuring frequency using the new phase error model, while the values remain relatively constant up to approximately 200 Hz and then decrease steeply with increasing frequency for the constant-phase error model. For the clay target, a spectrum continuously increasing with frequency is obtained with the new error model, while the constant-phase error model produces a spectrum with a phase maximum around 100 Hz. Although the true spectral signature of the targets is not known, with the constant-phase error model spectral responses are recovered which contradict expectations — this is not the case for the results obtained with the proposed error model. Copper in an electrolyte is known to produce a typical Cole-Cole phase response (e.g., Kemna et al., 2000), which obviously does not correspond to the observed flat and then abruptly decreasing phase response using the constant-phase error model. Clay is expected to show a response with increasing phase values up to the kHz range (e.g., Slater et al., 2006), as actually obtained with the new error model, but not consistent with the result using a constant-phase error model. These outcomes clearly demonstrate the sensitivity of imaged spectral characteristics with respect to the phase error description used in the inversion, and they suggest that the proposed phase error model produces more reliable results.

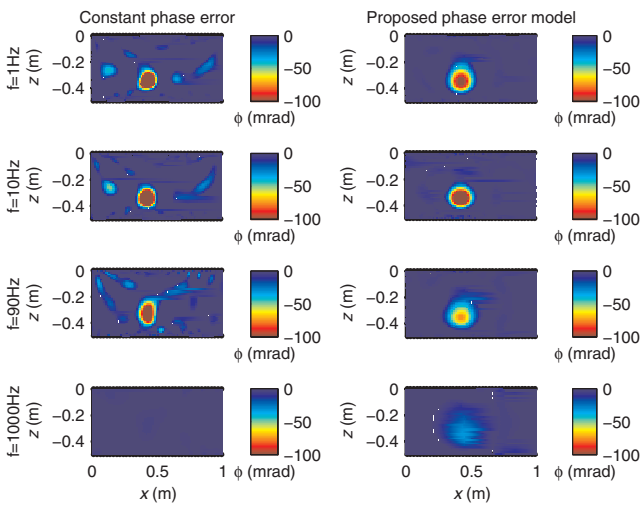

Figure 9. Resistivity phase images inverted from the tank data at different measurement frequencies using (left column) the constant-phase error model according to Slater and Binley (2006) and (right column) the proposed error model in equation 5 with parameters based on a multibin analysis.

APPLICATION TO SINGLE-FREQUENCY FIELD DATA

To validate our approach in a field-scale application, we reprocessed cross-borehole impedance data that were collected at the hydrological test site at Krauthausen, Germany (Kemna et al., 2004b), which is operated by Forschungszentrum Jülich. Several studies have been performed at the site, including electrical surveys, and its hydrogeologic characteristics are well known (see Kemna et al., 2002; Hördt et al., 2007; Tillmann et al., 2008; Müller et al., 2010).

Setup

Briefly, the area is defined by a 9 m thick aquifer, the basement of which is located at an approximate depth of 11 m. The aquifer is characterized by layers of gravel and sand corresponding to fluvial Rur sediments, overlain by a loess layer. For the impedance measurements, a total of five boreholes, defining a section of 27.5 m in length, were equipped with copper electrodes. Each borehole contains 13 electrodes between 3 and 9.5 m below ground surface (bgs), with an electrode separation of 0.5 m. Impedance magnitude and phase data were collected with the RESECS instrument by GeoServe at a frequency of 0.125 Hz. Measurements were performed between adjacent wells, using a skip-2 "cross dipoles" measurement protocol. Consistent with the tank measurements, data were collected in normal and reciprocal configurations, resulting — after rejection of obvious outliers — in a total of 706 magnitude and phase readings for the subsequent error analysis and inversion.

Results

The analysis of the field data revealed qualitatively the same distribution of normal-reciprocal discrepancies as a function of resistance as found for the laboratory data (Figure 11): a linear increase

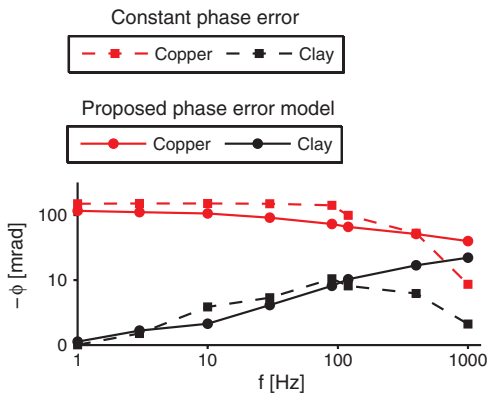

Figure 10. Spectral response for selected pixels of the inverted phase images of the tank model (see Figure 8) based on the constant-phase error model (triangles, dashed curves) and the proposed phase error model (circles, solid curves). Selected pixels correspond to the copper target (red) and the clay layer target (blue).

of the discrepancy in the resistance with resistance value, and an inverse power-law relationship between discrepancy in the phase and resistance value. Like the laboratory data, the field data were inverted using the resistance error model by LaBrecque et al. (1996), with parameters determined from the two different (single- and multibin) approaches and using the two different (constant-phase and power-law) error models for the phase. However, considering the smaller range of resistance values and the smaller number of measurements compared to the laboratory data sets, the multibin analysis was based on only six bins to determine the a and b parameters of the respective error models.

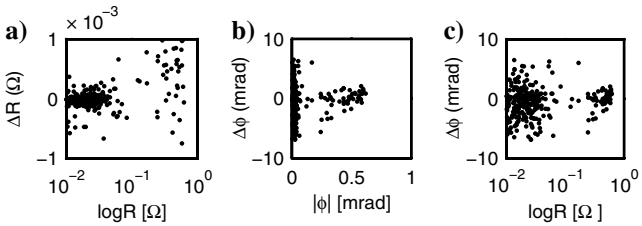

Figure 11. Raw field data collected at 0.125 Hz. (a) Normal-reciprocal resistance discrepancy versus log resistance. (b) Normal-reciprocal phase discrepancy versus absolute phase. (c) Normal-reciprocal phase discrepancy versus log resistance.

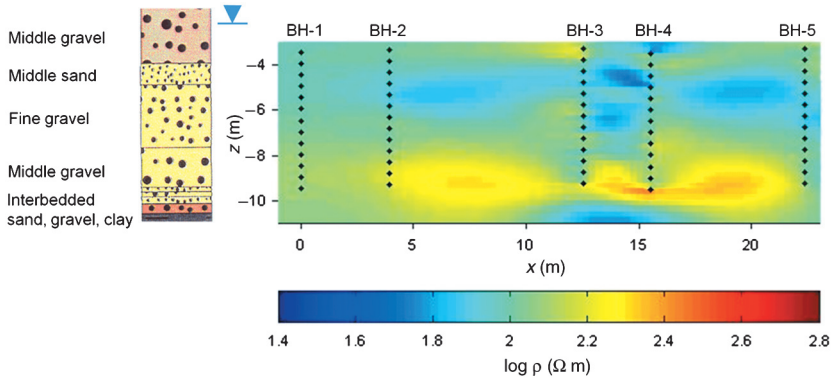

Figure 12. Resistivity magnitude image inverted from the field data using the error model in equation 4 with parameters based on the Slater and Binley (2006) approach. Solid circles indicate the position of electrodes in the five boreholes. Lithologic column of the Krauthausen site is shown on the left side (after Kemna et al., 2004b).

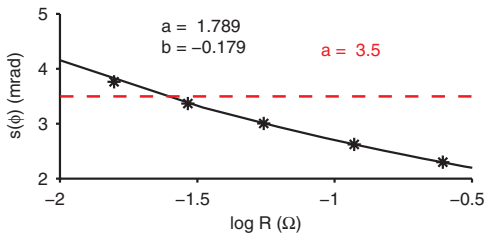

Figure 13. Phase error models for the field data based on the multibin analysis (black curve) and the single-bin approach (red line) by Slater and Binley (2006). The black dots indicate the standard deviations of the normal-reciprocal data discrepancies obtained in the individual bins. Also shown are the corresponding values of the error model parameters a and b (a in mrad and b value for R in Ω).

The obtained image of resistivity magnitude is again effectively the same for both methods of choosing the parameters of the error model, and hence only the result based on the single-bin analysis (a = 1 mΩ and b = 1.2%) is shown (Figure 12). The image reflects well the known geologic situation at the site. It exhibits a unit characterized by relatively low resistivity values (around 50 Ωm) located between 4 and 6 m bgs, which is embedded in a unit with moderate resistivity values (around 100 Ωm) extending down to 8 m depth. These units coincide with the known series of middle gravel, middle sand, and fine gravel layers. The high-resistive feature (around 250 Ωm) at the bottom of the image plane delineates a gravel unit at approximately 9 m depth, on top of interbedded strata of sand, gravel, and clay characterized by even lower resistivity values.

The phase error models obtained from the single-bin and multibin approaches are shown in Figure 13. Although the range of resistance values is much smaller than for the tank data (cf. Figures 6 and 7), a noticeable dependence of the phase error upon resistance is still observed for the multibin approach.

The corresponding phase images are shown in Figure 14. Both images are characterized by laterally continuous units. In general, the polarizability is weak and varies only between −2 and −6 mrad. The top layer reveals the highest absolute phase values (around −5 mrad) down to 5 to 6 m bgs, likely to be associated with a nonnegligible clay fraction in this region of middle gravel and middle sand (cf. Figure 12). Below is a low-polarizable (around −3 mrad), 2 to 3 m thick unit, corresponding to fine gravel, followed again by a subtle polarizability increase with depth in the middle gravel layer and below (cf. Figure 12). When comparing the two error model approaches, the low-polarizable unit is shown with better contrast for the new approach. This is obviously a consequence of the overall smaller phase error resulting from the multibin analysis (see Figure 13), meaning that the data are fitted to a higher degree. Although the difference in the phase imaging results for the two error models is less significant than for the tank data (because the range of measured resistances is much smaller), it nevertheless indicates the superiority of the new approach.

DISCUSSION

For tomographic data sets, high resistances are associated with high S/Ns (if the current is fairly constant). Thus it is reasonable to describe the error present in electrical impedance data sets as a function of resistance. Analogous to the case of impedance magnitude, in the previous sections we demonstrated the significant correlation between measured resistance and the phase error. Taking the observed dependency into account in the inversion by means of an appropriate error model helps to avoid the overfitting of phase data corresponding to low resistances and the underfitting of phase data corresponding to high resistances — as is the case for the assumption of a constant (i.e., independent of resistance) phase error (cf. Figure 6). The adequate parameterization of the error is particularly important for SIP data sets, independent of measurement

frequency. Although the overall error level typically increases with measurement frequency (see Figure 6), the problem of over- or underfitting remains the same. Accordingly, we find a rather erratic behavior of the recovered spectral response using a constant-phase error, while the images computed with the proposed error model provide a signature in agreement with expectations (Figure 10).

For the laboratory experiment, the true dimensions of the copper target might be viewed as being better resolved in the lower-frequency phase images obtained with a constant-phase error than in those obtained with the proposed error model (see Figure 9). However, this improved resolution is obtained at the cost of considerable artifacts in the images (and is a typical inversion phenomenon in the case of overfitting), which could easily lead to misinterpretations in the case of unknown targets. For the field study, we found an enhanced contrast (i.e., better resolution) in the phase images calculated with the proposed error model, without the occurrence of noticeable artifacts. This indicates that the proposed error model provides a fair compromise between image resolution and image reliability, in harmony with the philosophy of a smoothness-constraint inversion approach.

It is critical that the selected number of bins and their distribution ensure a homogeneous distribution of the data over the bins, to allow for a proper statistical analysis in each bin. In an initial data analysis step, obvious outliers, which may influence the chosen bin size and distribution, should be removed. Furthermore, the data points contained in each bin should exhibit a Gaussian distribution, to fulfill the assumption of a random error used in the inversion algorithm. The definition of an adequate number of bins may be particularly challenging for field data, where the total number of measurements may be considerably smaller than in our laboratory experiments. In addition, depending on the measuring protocol used, only a relatively narrow range of resistances may be covered, incapable of revealing the systematic dependence of phase error upon resistance. For a reliable determination of the parameters of the proposed error model, the resistance range in a data set should be as large as possible, obviously favoring dipole-dipole protocols or combinations thereof. However, even for the considered field data set, where resistances only varied over half an order of magnitude (see Figure 13), the proposed error model yields a phase image with improved contrast.

The inversion scheme used in this study is implemented in terms of the logarithm of impedance, mapping logarithm of resistance and phase into real and imaginary components of the data. An alternative approach is to directly invert the real (Z') and imaginary (Z'') components of impedance (e.g., Zimmermann et al., 2008, Commer et al., 2011). Accordingly, data error analysis and parameterization may also be performed in terms of real and imaginary components. However, both quantities scale with resistance, as they are given by

$$Z' = R \cos \phi, \tag{6}$$

$$Z' = R \sin \phi, \tag{7}$$

and thus it is plausible to again assume a systematic dependence of their errors upon resistance (note that for the typically low phase values in geophysical applications $Z' \approx R$ and $Z'' \approx R\phi$). Analogous to Figure 4, Figure 15 shows the distribution of the misfit between normal and reciprocal measurements collected on the experimental tank in terms of real and imaginary components (Z', Z''). Here, the discrepancy (between normal and reciprocal measurements) of the real and imaginary components plotted as a function of the real component ($\Delta Z'$, $\Delta Z''$ versus Z') exhibits a linear behavior, similar to the model of LaBrecque et al. (1996) (ΔR versus R) from equation 4. Based on this, we suggest that the model proposed by LaBrecque et al. (1996) may be adopted to describe the error for real and imaginary components

$$\Delta Z' = K_1 + K_2 Z', \tag{8}$$

$$\Delta Z'' = K_3 + K_4 Z', \tag{9}$$

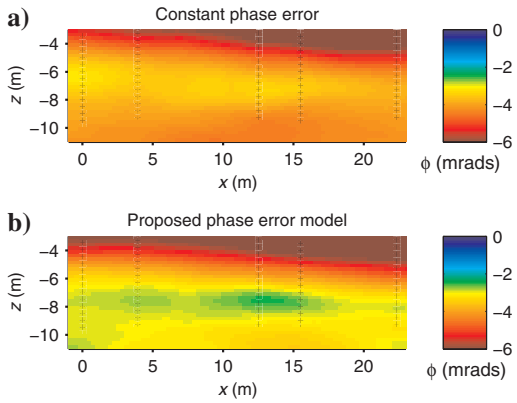

Figure 14. Resistivity phase images inverted from the field data using (a) the constant-phase error model according to Slater and Binley (2006) and (b) the proposed error model in equation 5 with parameters based on a multibin analysis. Solid circles indicate the positions of the electrodes in the five boreholes.

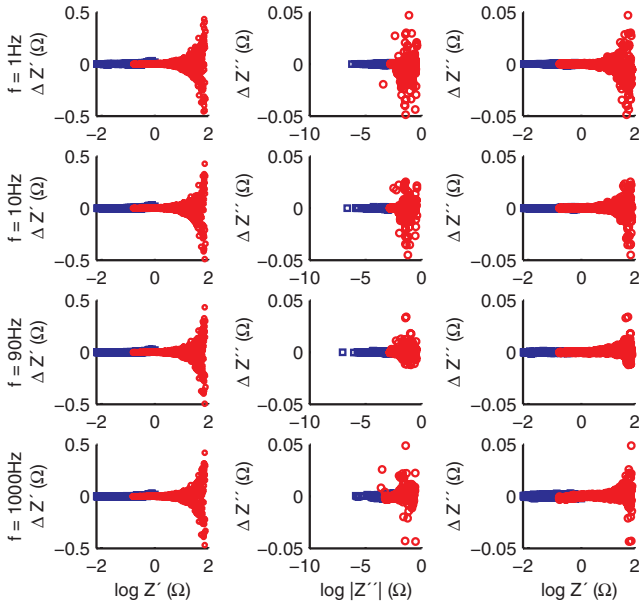

Figure 15. Raw tank data collected at different frequencies for both measurement schemes (blue squares: opposite dipoles; red circles: cross dipoles). Left column: Normal-reciprocal discrepancy in Z' versus log Z'. Middle column: Normal-reciprocal discrepancy in Z'' versus log $|Z''|$. Right column: Normal-reciprocal discrepancy in Z'' versus log Z'. Z' and Z'' denote, respectively, real and imaginary components of resistance.

where K_1, K_3 represent the absolute errors for the real and imaginary components, respectively, and K_2 and K_4 the respective relative errors. However, a further validation of this approach is beyond the scope of this study. Similar to the analysis of the magnitude and phase data, other relationships, for example the normal-reciprocal discrepancy in the imaginary component as a function of the absolute value of the imaginary component, did not provide any clear trend.

CONCLUSIONS

In this paper, we propose a new model to quantify the phase error in impedance data sets, as well as a methodology to compute the underlying parameters of the proposed error model. The analysis of impedance data sets collected in the laboratory and the field revealed a significant correlation between the discrepancy between normal and reciprocal phase measurements, on the one hand, and the corresponding mean resistance value, on the other hand. The observed behavior of decreasing phase discrepancy with increasing resistance is consistent for measurements collected at different frequencies, over a wide frequency range. Other dependences of the phase discrepancy, such as its dependence on the absolute phase value, also were studied, but did not show a similarly systematic behavior.

Based on the observed behavior of the phase discrepancy, we propose an inverse power-law relationship to describe the phase error as a function of resistance. Inversion of the considered data sets was performed with two error parameterization approaches, i.e., a constant-phase error and a new power-law model. The images computed with the power-law model demonstrated the advantage of the new parameterization as they showed fewer artifacts and, respectively, higher contrast than those obtained with the assumption of a constant-phase error. We attribute this to an underestimation of the error — and correspondingly an overfitting — of phase data associated with low resistances on the one hand, and an overestimation of the error — and correspondingly an underfitting — of phase data associated with high resistances on the other hand, when using the constant-error approach. The power-law model takes the observed variation in the phase error into account properly and provides improved images with a satisfying compromise between resolution and reliability (absence of artifacts). The latter aspect is particularly important if spectral characteristics are to be deduced from multifrequency phase images because spatial imaging artifacts may lead to significant distortions of spectral signatures, making a reliable interpretation impossible.

The quantification of phase data errors is critical for obtaining reliable phase images, and the proposed error model might represent an adequate parameterization of universal applicability. We consider an appropriate error description essential for quantitative IP/SIP imaging as it is increasingly becoming of interest, for instance, for hydrogeophysical and biogeophysical investigations. As far as monitoring applications are concerned, however, further studies are required concerning the most appropriate phase error model in a time-lapse inversion scheme.

ACKNOWLEDGMENTS

Adrián Flores Orozco thanks CONACyT and DAAD for the scholarship which allowed him to perform this work. Andreas Kemna gratefully acknowledges financial support from SFB/TR 32 (Patterns in Soil-Vegetation-Atmosphere Systems: Monitoring, Modeling, and Data Assimilation) funded by the Deutsche Forschungsgemeinschaft (DFG). This research was also made possible by funding received from the EU FP7 collaborative projects iSOIL (Interactions Between Soil Related Sciences — Linking Geophysics, Soil Science and Digital Soil Mapping) and ModelPROBE (Model Driven Soil Probing, Site Assessment and Evaluation). We thank the four anonymous reviewers for their constructive comments and the assistant editor Evert Slob for his additional, meticulous review, which helped to improve the manuscript.

REFERENCES

Bing, Z., and S. A. Greenhalgh, 2000, Cross-hole resistivity tomography using different electrode configurations: Geophysical Prospecting, **48**, 887–912, doi: 10.1046/j.1365-2478.2000.00220.x.

Binley, A., S. Kruschwitz, D. Lesmes, and N. Kettridge, 2010, Exploiting the temperature effects on low frequency electrical spectra of sandstone: A comparison of effective diffusion path lengths: Geophysics, **75**, no. 6, A43–A46, doi: 10.1190/1.3483815.

Binley, A., A. Ramirez, and W. Daily, 1995, Regularised image reconstruction of noisy electrical resistance tomography data: Proceedings of the 4th Workshop of the European Concerted Action on Process Tomography, 401–410.

Binley, A., L. D. Slater, M. Fukes, and G. Cassiani, 2005, Relationship between spectral induced polarization and hydraulic properties of saturated and unsaturated sandstone: Water Resources Research, **41**, W12417, doi: 10.1029/2005WR004202.

Commer, M., G. A. Newman, K. H. Williams, and S. S. Hubbard, 2011, 3D induced-polarization data inversion for complex resistivity: Geophysics, **76**, no. 3, F157–F171, doi: 10.1190/1.3560156.

Dahlin, T., V. Leroux, and J. Niessen, 2002, Measuring techniques in induced polarization imaging: Journal of Applied Geophysics, **50**, 279–298, doi: 10.1016/S0926-9851(02)00148-9.

Hördt, A., R. Blaschek, A. Kemna, and N. Zisser, 2007, Hydraulic conductivity estimation from induced polarization data at the field scale — The Krauthausen case history: Journal of Applied Geophysics, **62**, 33–46, doi: 10.1016/j.jappgeo.2006.08.001.

Hördt, A., A. Druiventak, R. Blaschek, F. Binot, A. Kemna, P. Kreye, and N. Zisser, 2009, Case histories of hydraulic conductivity estimation with induced polarization at the field scale: Near Surface Geophysics, **7**, 529–545.

Kemna, A., 2000, Tomographic inversion of complex resistivity — Theory and application: Ph.D. thesis, Ruhr University of Bochum.

Kemna, A., A. Binley, A. Ramirez, and W. Daily, 2000, Complex resistivity tomography for environmental applications: Chemical Engineering Journal (London), **77**, 11–18, doi: 10.1016/S1385-8947(99)00135-7.

Kemna, A., A. Binley, and L. Slater, 2004a, Crosshole IP imaging for engineering and environmental applications: Geophysics, **69**, 97–107, doi: 10.1190/1.1649379.

Kemna, A., J. Vanderborght, A. Englert, K. Müller, A. Tillmann, and H. Vereecken, 2004b, Characterization of structures and transport processes in a heterogeneous aquifer using electrical conductivity and induced polarization imaging: AGU Fall Meeting Abstracts, Abstract #H13G-02.

Kemna, A., J. Vanderborght, B. Kulessa, and H. Vereecken, 2002, Imaging and characterisation of subsurface solute transport using electrical resistivity tomography (ERT) and equivalent transport models: Journal of Hydrology, **267**, 125–146, doi: 10.1016/S0022-1694(02)00145-2.

Koestel, J., A. Kemna, M. Javaux, A. Binley, and H. Vereecken, 2008, Quantitative imaging of solute transport in an unsaturated and undisturbed soil monolith with 3-D ERT and TDR: Water Resources Research, **44**, W12411, doi: 10.1029/2007WR006755.

LaBrecque, D. J., and W. Daily, 2008, Assessment of measurement errors for galvanic-resistivity electrodes of different composition: Geophysics, **73**, no. 2, F55–F64, doi: 10.1190/1.2823457.

LaBrecque, D. J., M. Miletto, W. Daily, A. Ramirez, and E. Owen, 1996, The effects of noise on Occam's inversion of resistivity tomography data: Geophysics, **61**, 538–548, doi: 10.1190/1.1443980.

Militzer, H., and F. Weber, 1985, Angewandte Geophysik, Band 2 — Geoelektrik, Geothermik, Radiometrie, Aerogeophysik: Springer.

Müller, K., J. Vanderborght, A. Englert, A. Kemna, J. A. Huisman, J. Rings, and H. Vereecken, 2010, Imaging and characterization of solute transport during two tracer tests in a shallow aquifer using electrical resistivity tomography and multilevel groundwater samplers: Water Resources, **46**, W03502, doi: 10.1029/2008WR007595.

Pelton, W. H., S. H. Ward, P. G. Hallof, W. R. Sill, and P. H. Nelson, 1978, Mineral discrimination and inductive coupling removal with multifrequency IP: Geophysics, **43**, 588–609, doi: 10.1190/1.1440839.

Ramirez, A., W. Daily, and D. LaBrecque, 1999, Electrical impedance tomography of known targets: Journal of Environmental and Engineering Geophysics, **4**, 11–26, doi: 10.4133/JEEG4.1.11.

Revil, A., and N. Florsch, 2010, Determination of permeability from spectral induced polarization in granular media: Geophysical Journal International, **181**, 1480–1498, doi: 10.1111/j.1365-246X.2010.04573.x.

Slater, L., and A. Binley, 2006, Synthetic and field-based electrical imaging of zerovalent iron barrier: Implications for monitoring long-term barrier performance: Geophysics, **71**, no. 5, B129–B137, doi: 10.1190/1.2235931.

Slater, L., A. Binley, W. Daily, and R. Johnson, 2000, Cross-hole electrical imaging of a controlled saline tracer injection: Journal of Applied Geophysics, **44**, 85–102, doi: 10.1016/S0926-9851(00)00002-1.

Slater, L., D. Ntarlagiannis, and D. Wishart, 2006, On the relationship between induced polarization and surface area in metal-sand and clay-sand mixtures: Geophysics, **71**, no. 2, A1–A5, doi: 10.1190/1.2187707.

Slater, L. D., D. Ntarlagiannis, F. D. Day-Lewis, K. Mwakanyamale, R. J. Versteeg, A. Ward, C. Strickland, C. D. Johnson, and J. W. Lane Jr., 2010, Use of electrical imaging and distributed temperature sensing methods to characterize surface water-groundwater exchange regulating uranium transport at the Hanford 300 Area, Washington: Water Resources Research, **46**, W10533, doi: 10.1029/2010WR009110.

Stummer, P., H. Maurer, and A. G. Green, 2004, Experimental design: Electrical resistivity data sets that provide optimum subsurface information: Geophysics, **69**, 120–139, doi: 10.1190/1.1649381.

Tillmann, A., A. Englert, Z. Nyari, I. Fejes, J. Vanderborght, and H. Vereecken, 2008, Characterization of subsoil heterogeneity, estimation of grain size distribution and hydraulic conductivity at the Krauthausen test site using cone penetration test: Journal of Contaminant Hydrology, **95**, 57–75, doi: 10.1016/j.jconhyd.2007.07.013.

Weidelt, P., and A. Weller, 1997, Computation of geoelectrical configuration factors for cylindrical core samples: Scientific Drilling, **6**, 27–34.

Williams, K. H., A. Kemna, M. J. Wilkins, J. Druhan, E. Arntzen, A. L. N'Guessan, P. E. Long, S. S. Hubbard, and J. F. Banfield, 2009, Geophysical monitoring of coupled microbial and geochemical processes during stimulated subsurface bioremediation: Environmental Science and Technology, **43**, 6717–6723, doi: 10.1021/es900855j.

Wong, J, 1979, An electrochemical model of the induced polarization phenomenon in disseminated sulfide ores: Geophysics, 44, 1245–1265, doi: 10.1190/1.1441005.

Xu, B., and M. Noel, 1993, On the completeness of data sets with multielectrode systems for electrical resistivity survey: Geophysical Prospecting, **41**, 791–801, doi: 10.1111/gpr.1993.41.issue-6.

Zimmermann, E., A. Kemna, J. Berwix, W. Glaas, and H. Vereecken, 2008, EIT measurement system with high phase accuracy for the imaging of spectral induced polarization properties of soils and sediments: Measurement Science and Technology, **19**, 094010, doi: 10.1088/0957-0233/19/9/094010.

Zisser, N., A. Kemna, and G. Nover, 2010, Relationship between low-frequency electrical properties and hydraulic permeability of low-permeability sandstones: Geophysics, **75**, no. 3, E131–E141, doi: 10.1190/1.3413260.